Beyond LISA: Exploring future gravitational wave missions

Jeff Crowder and Neil J. Cornish

Department of Physics, Montana State University, Bozeman, Montana 59717, USA
(Received 17 June 2005; published 20 October 2005)

The Advanced Laser Interferometer Antenna (ALIA) and the Big Bang Observer (BBO) have been proposed as follow on missions to the Laser Interferometer Space Antenna (LISA). Here we study the capabilities of these observatories, and how they relate to the science goals of the missions. We find that the Advanced Laser Interferometer Antenna in Stereo (ALIAS), our proposed extension to the ALIA mission, will go considerably further toward meeting ALIA's main scientific goal of studying intermediate mass black holes. We also compare the capabilities of LISA to a related extension of the LISA mission, the Laser Interferometer Space Antenna in Stereo (LISAS). Additionally, we find that the initial deployment phase of the BBO would be sufficient to address the BBO's key scientific goal of detecting the Gravitational Wave Background, while still providing detailed information about foreground sources.

I. INTRODUCTION

The launch of the Laser Interferometer Space Antenna (LISA) [1] in the next decade will usher in a new era for gravitational wave detection. LISA will not only detect the presence of gravitational waves, but also provide detailed information about many thousands of gravitational wave sources, vastly expanding the burgeoning field of gravitational wave astronomy.

The primary sources for LISA are expected to be compact galactic binaries [2], supermassive black hole binaries, and extreme mass ratio inspirals. The gravitational wave signals detected by LISA encode information about the parameters of the binary systems, such as sky locations, masses, and distances, which can be extracted by matched filtering. Studies into the accuracy with which the source parameters can be recovered from the LISA data have been performed for compact galactic binaries [3–6], supermassive black hole binaries [3,4,7–9], and extreme mass ratio inspirals [10].

It is hoped that LISA will be the first of several efforts to explore the low frequency portion of the gravitational wave spectrum accessible to space-borne interferometers. One possible follow on mission is tentatively named the Advanced Laser Interferometer Antenna (ALIA) [11], featuring a spacecraft configuration similar to that of LISA, with smaller arm lengths and lower noise levels. The primary mission of ALIA will be detecting intermediate mass black holes (IMBHs), with masses in the range 50–$50\,000 M_\odot$. Information on populations, locations, and event rates could greatly enhance theories of black hole formation and evolution. Another proposed follow on mission is the Big Bang Observer [12] (BBO). The BBO will be an extremely sensitive antenna that is designed to detect the Gravitational Wave Background (GWB) left by the Big Bang. According to the standard cosmological picture, the GWB is a relic of the early inflationary period of the Universe. Just as the COsmic Background Explorer (COBE) and the Wilkinson Microwave Anisotropy Probe

(WMAP) missions provided information about the Universe around the time of last scattering, the BBO should be able to provide information about the earliest moments in the history of the Universe. The current BBO proposal calls for four LISA-like spacecraft constellations, with the orbital configuration shown in Fig. 1. Two of the constellations will be centered on a 20° Earth-trailing orbit, rotated 60° with respect to each other in the plane of the constellations. These constellations will be referred to as the star constellations, as the legs of the constellation sketch out a six pointed star. The remaining two constellations are to be placed in an Earth-like orbit 120° ahead and behind the star constellations. These two constellations will be referred to as the outrigger constellations. The purpose of the outrigger constellations is to provide greater angular resolution for foreground sources (see Sec. III for details). The star constellations provide maximum cross-correlation of gravitational wave signals between the two constellations, with minimal correlated noise [13]. The noise in each detector is expected to be independent, so over time the overlap of the noise between the two constellations will tend to average to zero, while the overlap of the signal will grow. The plan is to deploy the BBO in
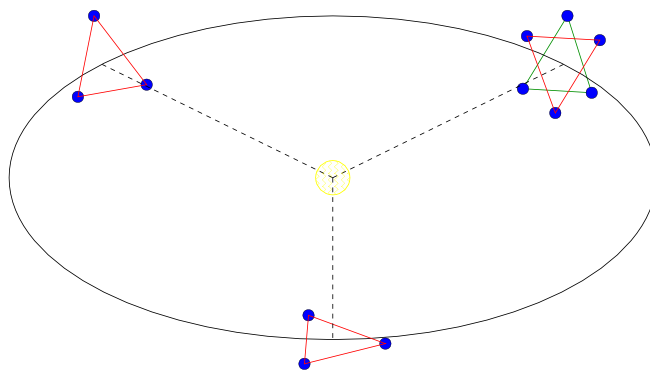

FIG. 1 (color online). The proposed orbital configuration of the Big Bang Observer.

stages, starting with the star constellation, then adding the outrigger constellations at a later date.

Figure 2 shows the detector sensitivities for LISA, ALIA, and BBO, a level for the expected extragalactic background confusion noise [14], and optimally filtered amplitude plots for equal mass binaries in their last year before coalescence at redshift $z = 1$. The squares shown on the amplitude plots denote the frequency of the signal one week before coalescence. The signal from coalescing equal mass binaries at $z = 1$ with masses above $10^1 M_\odot$ will be detectable by both ALIA and BBO. The BBO will also be able to detect lower mass systems such as neutron star (NS) binaries. However, for coalescing binaries, a large portion of the signal strength is due to the rapid inspiral in the last week, and for $10 M_\odot$ binaries at $z = 1$ or greater, much of this power is deposited after the signal has crossed the ALIA sensitivity curve.

Here we begin by analyzing the parameter resolution of ALIA for IMBHs. These studies indicate that by including a second identical constellation of spacecraft in a 20° Earth-leading orbit, providing a constellation separation of 40°, the parameter resolution will be greatly improved. We will call this two constellation configuration the Advanced Laser Interferometer Antenna in Stereo (ALIAS). We will also address the natural question, given the increases in precision that ALIAS provides relative to ALIA, what would be gained by adding a second constellation to the LISA mission—the Laser Interferometer Space Antenna in Stereo (LISAS). Lastly, we analyze the parameter resolution of the BBO for NSs, $10 M_\odot$, and $100 M_\odot$ black holes (BHs), and for the initial deployment phase of the BBO, which we call BBO Star, containing the two star constellations of the BBO configuration, but not the outrigger constellations. We will show that parameter resolu-

tion of the BBO and BBO Star should be sufficient to detect foreground binary systems, out to and beyond a redshift of $z = 3$.

This paper is organized as follows. We begin with a review of parameter estimation in Sec. II. In Sec. III we describe how a pair of well separated detectors can significantly improve the angular resolution for transient sources. This is followed by our study of the ALIA mission in Sec. IV A, and a study of our dual-detector variant of the ALIA mission in Sec. IV B. Results for unequal mass binaries for ALIA and ALIAS are in Sec. IV C. The LISA and LISAS missions are compared in Sec. IV D. The BBO mission is studied in Sec. IV E, and results for a down-scoped version of the BBO mission are reported in Sec. IV F. Concluding remarks are made in Sec. V.

II. REVIEW OF PARAMETER ESTIMATION

In our analysis, the orbits of the binaries are treated as quasicircular and spin effects are neglected. This leaves nine parameters that will describe the binary systems: sky location (θ, ϕ); inclination and polarization angles (ι, ψ); reduced and chirp masses $(\mu, \mathcal{M})$; time to coalescence (t_c), luminosity distance (D_L), and the initial orbital phase (γ_o). The signals are modeled using a truncated second-Post Newtonian (2PN) approximation [15] whereby the amplitude is kept to Newtonian order while the phase is kept to second order. In other words, we only include the dominant second harmonic of the orbital frequency.

The response of a space-borne instrument to a gravitational wave source is encoded in the Michelson-like time-delay interferometry (TDI) variables [16], $X_i(t)$. Here the subscript i denotes the vertex at which the signal is read out. In the equal-armlength limit, the TDI signal, $X_i(t)$, can be formed from a time-delayed combination of Michelson signals, $M_i(t)$, by

$$X_i(t) = M_i(t) - M_i(t - 2L). \tag{1}$$

This differencing cancels the laser phase noise, while preserving the gravitational wave signal. Rather than work with the correlated $X_i(t)$ variables directly, we use the orthogonal signal combinations [17]

$$A(t) = \sqrt{\frac{3}{2}}(S_{II}(t) - S_{II}(t - L)),$$
$$E(t) = \sqrt{\frac{3}{2}}(S_I(t) - S_I(t - L)), \tag{2}$$

where

$$S_I(t) = \frac{1}{3}(2M_1(t) - M_2(t) - M_3(t)),$$
$$S_{II}(t) = \frac{1}{\sqrt{3}}(M_2(t) - M_3(t)). \tag{3}$$

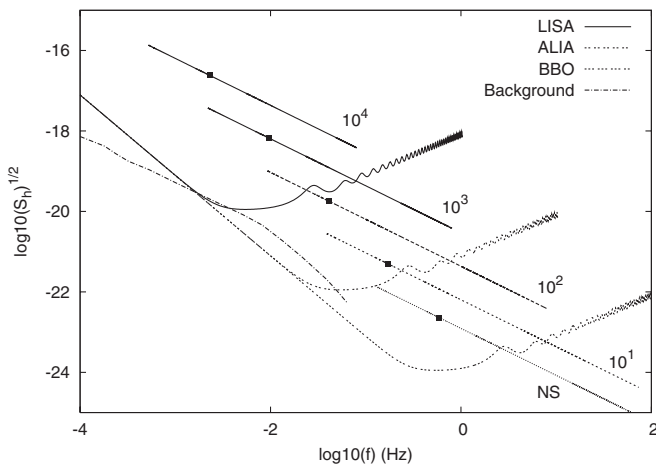The A, E combinations cancel the laser phase noise that

FIG. 2. Sensitivity curves for LISA, ALIA, and BBO with optimally filtered amplitude plots for equal mass binaries at $z = 1$ in their last year before coalescence. The masses shown are in units of solar masses. The squares denote the frequency one week from coalescence.
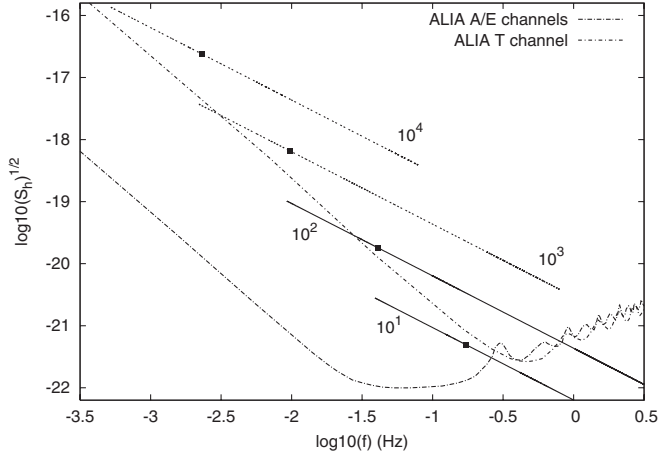
FIG. 3. Sensitivity curves for the A, E, and T channels for ALIA with optimally filtered amplitude plots for equal mass binaries at $z = 1$ in their last year before coalescence. The masses shown are in units of solar masses. The squares denote the frequency one week from coalescence.

would otherwise dominate the Michelson signals. At high frequencies, $f > f_* \equiv c/(2\pi L)$, where L is the length of the detector arms, a third independent data channel $T(t)$ becomes available. For frequencies below f_* the T-channel is insensitive to gravitational waves and can be used as an instrument noise monitor. To simplify our analysis we did not use the T-channel. Including this channel would not have had much effect on the trend of our results. As an example, looking at Fig. 3 one can see that for ALIA inclusion of the T-channel has little to no effect for binaries $< 10^2 M_\odot$. Higher mass binaries would have marginally improved signal strength and correspondingly improved resolution of the parameters. Table I contains signal-to-noise ratio (SNR) information for the combined A and E channels, as well as the T channel for equal mass binaries as seen by ALIA in the year before coalescence. The SNRs in Table I are for the final year before coalescence, separated into the contribution from the first 51 weeks and the contribution from the final week.

In the low frequency limit, the variables S_I and S_{II} reduce to the independent data channels defined by Cutler [3]. We use the rigid adiabatic approximation [18] to model the gravitational wave content of the data channels. The instrument noise in the A and E channels was

TABLE I. SNRs for the T channel and the combined SNRs for the A and E channels as seen by ALIA for the equal mass binaries located at $z = 1$.

	51 week SNR		Last week SNR	
	$A + E$	T	$A + E$	T
$10^2 M_\odot$	44.6	0.599	16.0	2.29
$10^3 M_\odot$	122	1.23	302	16.1
$10^4 M_\odot$	131	3.52	2145	34.8

modeled by [17,19]

$$S_n(f) = 8\sin^2(f/2f_*)\bigg[(2 + \cos(f/f_*))S_{\text{pos}}$$
$$+ 2(3 + 2\cos(f/f_*)$$
$$+ \cos(2f/f_*))\frac{S_{\text{accl}}}{(2\pi f)^4}\bigg]\bigg/(2L)^2,$$

where S_{pos} and S_{accl} are the one-way position and acceleration noise contributions. Table II lists the instrument parameters used in our study of the LISA, ALIA and BBO missions.

The A and E signals are functions of the nine parameters $\vec{\lambda} \to (\theta, \phi, t_c, D_L, \iota, \psi, \mathcal{M}, \mu, \gamma_\mathcal{O})$ that describe the source. The source parameters can be recovered from the data channels using a variety of data analysis methods. We will consider maximum likelihood estimation, using the log likelihood function

$$\log\mathcal{L}(\vec{\lambda}') = (s|h(\vec{\lambda}')) - \frac{1}{2}(h(\vec{\lambda}')|h(\vec{\lambda}')), \qquad (4)$$

where s denotes the data and $h(\vec{\lambda}')$ denotes the search template. We use the standard noise-weighted inner product $(a|b)$ summed over the independent data channels:

$$(a|b) = 2\sum_{A,E}\int_0^\infty \frac{a^*(f)b(f) + a(f)b^*(f)}{S_n(f)}df. \qquad (5)$$

For our work here the limits of the integration are set by the initial and cutoff frequencies of the binary systems. To first order these are given by

$$f_{\text{initial}} = 3.1\bigg(\frac{10^3 M_\odot}{\mathcal{M}(1 + z)}\bigg)^{5/8} \text{ mHz}, \qquad (6)$$

$$f_{\text{cut-off}} = 4.4\bigg(\frac{10^3 M_\odot}{M_{\text{total}}(1 + z)}\bigg) \text{ Hz}, \qquad (7)$$

where $M_{\text{total}} = \mathcal{M}^{5/2}/\mu^{3/2}$ is the total binary mass. Setting $\vec{\lambda}'$ equal to the true source parameters yields the SNR

$$\text{SNR}^2 = 2\langle\log\mathcal{L}(\vec{\lambda})\rangle = (h(\vec{\lambda})|h(\vec{\lambda})). \qquad (8)$$

Here the angle brackets $\langle\,\rangle$ denote an expectation value. The maximum likelihood estimator $\vec{\lambda}_{\text{ML}}$ is defined by

$$\frac{\partial \log\mathcal{L}(\vec{\lambda}_{\text{ML}})}{\partial \lambda^i} = 0. \qquad (9)$$

TABLE II. Instrument parameters.

Parameter	LISA	ALIA	BBO
$S_{\text{pos}}(\text{m}^2\,\text{Hz}^{-1})$	4×10^{-22}	1×10^{-26}	2×10^{-34}
$S_{\text{accel}}(\text{m}^2\,\text{s}^{-4}\,\text{Hz}^{-1})$	9×10^{-30}	9×10^{-32}	9×10^{-34}
$L(\text{m})$	5×10^9	5×10^8	5×10^7

The Fisher Information Matrix (FIM), Γ, is given as the negative of the expectation value of the Hessian evaluated at maximum likelihood:

$$\Gamma_{ij} = -\left\langle \frac{\partial^2 \log \mathcal{L}(\vec{\lambda}_{\mathrm{ML}})}{\partial \lambda^i \partial \lambda^j} \right\rangle = (h_{,i}|h_{,j}), \qquad (10)$$

where $h_{,i} \equiv \frac{\partial h}{\partial \lambda^i}$. For large SNR, the parameter estimation uncertainties, $\Delta \lambda^i$, will have the Gaussian probability distribution

$$p(\Delta \lambda^i) = \sqrt{\frac{\det \Gamma}{(2\pi)^9}} \exp\left(-\frac{1}{2}\Gamma_{ij}\Delta\lambda^i\Delta\lambda^j\right), \qquad (11)$$

and variance-covariance matrix

$$\langle \Delta\lambda^i \Delta\lambda^j \rangle = C^{ij} = (\Gamma^{-1})^{ij}. \qquad (12)$$

The uncertainties in each of the parameters are given by $\Delta\lambda^i = (C^{ii})^{1/2}$ (no summation). One can see from Eqs. (5) and (12) that the parameter uncertainties scale inversely with the SNR.

III. MULTIPLE CONSTELLATION DETECTION

Detectors such as LISA and ALIA determine the positions of gravitational wave sources through both amplitude and frequency modulation. The angular resolution improves with time due to the accumulation of SNR and the synthesis of a long baseline as the detectors move in their orbit. In contrast, a detector array like the BBO has widely separated elements, and thus has a built-in baseline. Adding a second widely separated constellation to LISA or ALIA would increase the SNR by a factor of $\sqrt{2}$, but the main gain in angular resolution for transient sources would be due to the built-in baseline. The advantage of a multi-element array can be understood from the following toy model. Suppose that we have a gravitational wave of known amplitude and frequency. Neglecting the effects of amplitude modulation we have

$$h = A\cos(2\pi f(t + R\sin(\theta)\cos(2\pi f_m t + \kappa - \phi))). \qquad (13)$$

Here f is the source frequency, R is the distance from solar barycenter to the guiding center of the constellation, $f_m = 1/\mathrm{year}$ is the modulation frequency, κ is the azimuthal location (along Earth's orbit) of the guiding center, and θ and ϕ give the source location on the sky.

With this two parameter (θ and ϕ) signal, we can analytically derive the uncertainty in the solid angle for a source observed for a time, T_{obs}, by a single constellation

$$\Delta\Omega_{\mathrm{single}} = \frac{2S_n(f)}{(A\pi f R)^2 \sin(2\theta)T_{obs}}$$
$$\times \frac{1}{\sqrt{(1 - \mathrm{sinc}^2(2\pi f_m T_{obs}))}}. \qquad (14)$$

For small observation times $\Delta\Omega_{\mathrm{single}}$ scales as T_{obs}^{-2}, while for large observation times it scales as T_{obs}^{-1}.

Turning to the dual-detector case, we simply add together the FIMs for each individual detector. For two constellations separated by an angle $\Delta\kappa$, this yields a solid angle uncertainty of

$$\Delta\Omega_{\mathrm{dual}} = \frac{S_n(f)}{(A\pi f R)^2 \sin(2\theta)T_{obs}}$$
$$\times \frac{1}{\sqrt{(1 - \mathrm{sinc}^2(2\pi f_m T_{obs})\cos^2(\Delta\kappa))}}. \qquad (15)$$

For small observation times and nonzero $\Delta\kappa$, $\Delta\Omega_{\mathrm{dual}}$ scales as T_{obs}^{-1}. In other words, the built-in baseline leads to a much improved angular resolution for short observation times. This is very important for coalescing binaries as most of the SNR accumulates in the final days or weeks prior to merger. Note that if the two constellations are colocated, $\Delta\kappa = 0$, the uncertainty in the solid angle is reduced by a factor of 2 relative to the single detector case by virtue of the increased SNR. Also, note that this toy model only includes Doppler modulation, thus the symmetry between $\Delta\kappa = 0$ and $\Delta\kappa = \pi$. Including the amplitude modulation breaks this symmetry.

IV. RESULTS

The data shown here is for sources at a redshift of $z = 1$ for ALIA, ALIAS, LISA, and LISAS and redshift $z = 3$ for BBO, and BBO Star. These correspond to luminosity distances of 6.63 Gpc and 25.8 Gpc, respectively, using the best fit WMAP cosmology [20]. Each binary system is observed for the last year before coalescence. Each data point is distilled from 10^5 random samples of θ, ϕ, ι, ψ, and γ_o. For t_c, D_L, $\mathcal{M}$, and μ, we use logarithmic derivatives so that the uncertainties listed have been scaled by the value of the parameters. The uncertainty in sky location is simply the root of the solid angle uncertainty ($\sqrt{\Delta\Omega}$). The remaining angular parameters, ι, ψ, and γ_o, have not been scaled.

The angular variables were chosen by using a Monte Carlo method. The values for $\cos(\theta)$ and $\cos(\iota)$ were chosen from a random draw on $[-1, 1]$. Values for ϕ, ψ, and γ_o were each chosen from random draws on $[0, 2\pi]$. The parameters $\mathcal{M}$ and D_L were set for each Monte Carlo run (though they changed between runs). Time to coalescence, t_c, was set to 1 year plus a small offset so that during the year of observation the binary did not reach a relativistic regime that would not be properly modeled by the $2PN$ approximations used.

The mean SNRs quoted in this paper are calculated by taking the square root of the average of the squares of the individual SNRs. For our analysis, positive detection will be restricted to SNRs above 5.

TABLE III.   SNR and parameter uncertainties for ALIA with sources at $z = 1$.

	$10^2 M_\odot$		$10^3 M_\odot$		$10^4 M_\odot$		$10^5 M_\odot$	
	Median	Mean	Median	Mean	Median	Mean	Median	Mean
SNR	71.7	76.2	466	567	2937	3641	6481	7970
Sky location	0.169°	0.201°	0.234°	0.264°	0.382°	0.417°	0.518°	0.546°
$\ln(t_c) \times 10^{-8}$	1.38	1.58	2.74	3.11	4.41	5.16	5.38	6.47
$\ln(\mathcal{M}) \times 10^{-8}$	9.56	11.0	12.1	13.9	31.3	35.7	136	152
$\ln(\mu) \times 10^{-5}$	46.8	53.6	5.10	5.86	1.76	2.03	2.66	3.03
$\ln(D_L) \times 10^{-2}$	6.25	32.7	1.34	6.44	1.08	3.50	1.15	3.08
ι	3.99°	125°	0.762°	22.4°	0.513°	8.00°	0.515°	5.66°
ψ	5.44°	1092°	1.08°	176°	0.840°	42.3°	0.931°	24.7°
γ_o	12.2°	2185°	4.15°	352°	2.79°	85.4°	2.51°	50.0°

A. Results for ALIA

Table III summarizes the medians and means of parameter uncertainties for detections by ALIA of equal mass binaries with masses of $10^2 M_\odot$, $10^3 M_\odot$, $10^4 M_\odot$, and $10^5 M_\odot$. The SNRs for this range of masses shows that ALIA should get positive detection of $99^+\%$ of coalescing IMBHs located at $z = 1$ or closer, which would provide good information on the coalescence rates. The great precision in the measurement of $\mathcal{M}$ and μ will provide a clear picture of the constituent masses of the binary systems. Furthermore, the subdegree precision in the sky location, combined with luminosity distances known to a few percent, will facilitate the construction of a three dimensional distribution of IMBHs with which to test theoretical predictions (see Ref. [21] for a related discussion concerning LISA and supermassive black holes).

The uncertainties in t_c a month from coalescence (using 11 months of data) will be on the order of a few minutes. This will provide warning time for ground-based gravitational wave detectors, as well as other systems (telescopes, neutrino detectors, etc.) to gather as much and as varied data as possible about the coalescence.

The shapes of the histograms shown in Fig. 4, which are from the $10^3 M_\odot$ data, are representative of the histograms for each of the detectors covered in this work. Note that for ι, ψ, and γ_o, the tails of the histograms run far beyond the range of the plots shown, raising the values of the means considerably above their respective median values. For example, while the median value of γ_o for equal mass binaries with masses $10^2 M_\odot$ is 12.2°, its mean value is 2185°, which is well beyond the $[0, 2\pi]$ range of γ_o. Uncertainty ranges that are larger than the possible range of the parameter tell us that the parameter is indeterminate.
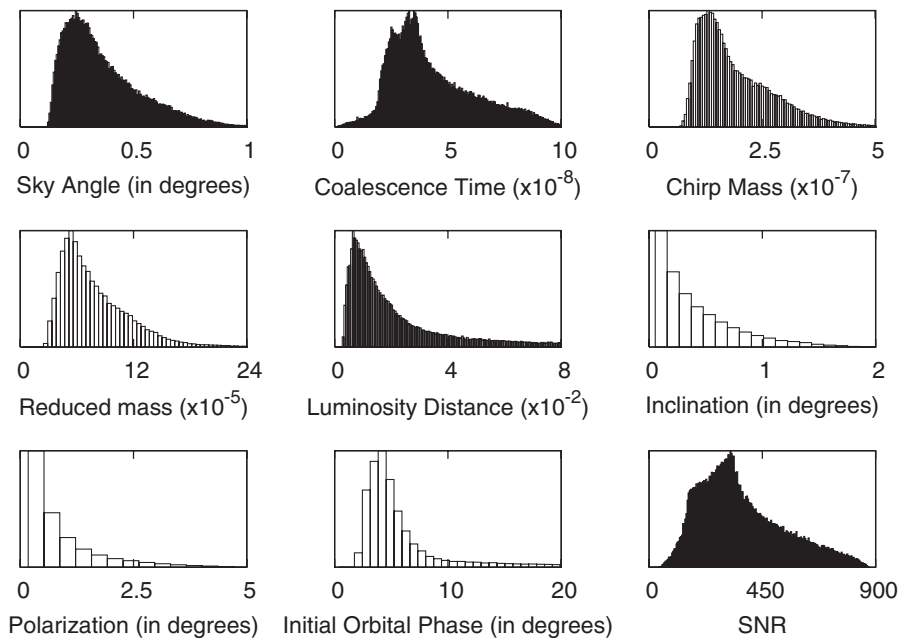

FIG. 4.   Histograms of the parameter uncertainties and SNR, for equal mass binaries of $10^3 M_\odot$ at $z = 1$, as detected by ALIA.
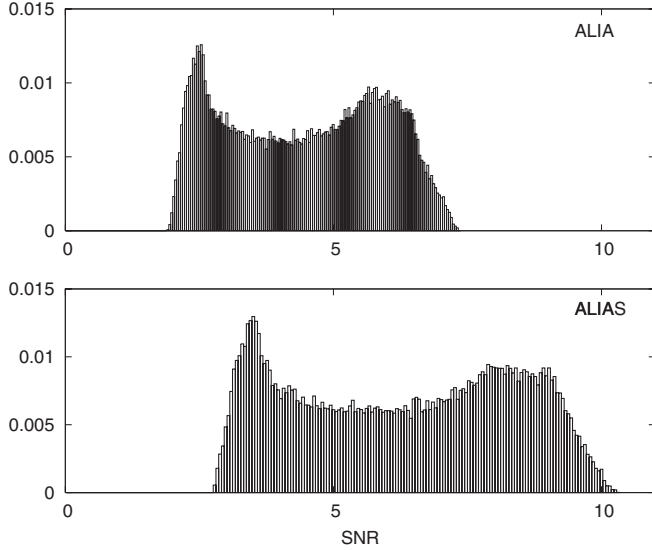
FIG. 5. SNR histogram for ALIA and ALIAS from $10M_\odot$ equal mass binaries at $z = 1$.

When uncertainty ranges exceed the possible range of a parameter, one may drop that parameter from the FIM analysis. For our analysis, we did not discard any parameters. As an example of how this affects the analysis, consider the $10^2 M_\odot$ study where the mean value of the uncertainties that lie in the $[0, 2\pi]$ range for γ_o would be $36.3°$, while its median would be $9.79°$. However, for 16.9% of the binaries, the γ_o parameter would be indeterminate.

Figure 5 shows the SNR histograms for $10M_\odot$ equal mass binaries for ALIA (and ALIAS). As was expected from Fig. 2, the SNR values for ALIA are low, with nearly 60% too low for a positive detection. Of note, though, is that the SNR scales roughly as the luminosity distance. This suggests that ALIA should be able to detect nearly all $10M_\odot$ binaries with luminosity distances less than 2 Gpc. For binaries with masses beyond $15M_\odot$, the low end of the range of SNRs is above 5, meaning that equal mass binaries with masses in the range of IMBHs should be detectable out to $z = 1$.

B. Results for ALIAS

The main purpose of ALIA is gathering information about IMBHs; our data shows it is capable of doing this with some success. A more accurate IMBH census could be derived from a dual constellation version of ALIA that we call ALIA in Stereo or ALIAS. Each component of the ALIAS constellation would be offset from the Earth by $20°$, one in an Earth-trailing and the other in an Earth-leading orbit, giving a $40°$ separation in order to provide increased parameter resolution in the IMBH range.

Table IV summarizes the medians and means of the parameter resolutions that could be achieved by the ALIAS mission. Results are given for equal mass binaries with masses of $10^2 M_\odot$, $10^3 M_\odot$, $10^4 M_\odot$, and $10^5 M_\odot$. As expected, the mean SNR increases by $\sqrt{2}$ relative to ALIA. The improvements in parameter resolution are, however, considerably larger. At the upper end of the IMBH mass range, the angular resolution improves by a factor of ~ 90 and the luminosity distance resolution improves by a factor of ~ 23.

For masses below $\sim 10^2 M_\odot$, ALIAS provides roughly a factor of $\sqrt{2}$ increase in the median values of each of the parameter uncertainties. This can be seen in the $10^2 M_\odot$ data in Tables III and IV, as well as in Figs. 6 and 7, which plot the uncertainty in the sky location and luminosity distance, respectively, against the chirp mass of the binaries. The trend shown in these figures holds true for D_L, ι, and ψ in that mass range, while the increases in t_c, μ, γ_o, and $\mathcal{M}$ are slightly larger, ~ 1.55 better than the values for ALIA. However, the median SNRs are below 5 for equal mass binaries with chirp masses below $\sim 8M_\odot$ for ALIAS (below $\sim 10M_\odot$ for ALIA).

Figure 6 also shows that the benefits of a dual constellation becomes even more significant when the final chirp of the binary occurs above the detector noise (see Fig. 2). The main improvement is in the angular resolution, but the decreased covariances between the sky location and other parameters lead to improved measurements of t_c, D_L, ι, and ψ at the upper end of the IMBH mass range. The resolution of these parameters improves (relative to

TABLE IV. SNR and parameter uncertainties for ALIAS with sources at $z = 1$.

|	$10^2 M_\odot$		$10^3 M_\odot$		$10^4 M_\odot$		$10^5 M_\odot$	
	Median	Mean	Median	Mean	Median	Mean	Median	Mean
SNR	102	108	688	802	4402	5164	9630	11 371
Sky location	$0.0620°$	$0.0769°$	$0.0284°$	$0.0330°$	$0.007\,86°$	$0.009\,05°$	$0.007\,57°$	$0.008\,46°$
$\ln(t_c) \times 10^{-9}$	7.84	9.01	10.6	11.9	3.33	4.42	2.19	2.82
$\ln(\mathcal{M}) \times 10^{-8}$	6.04	6.86	6.64	7.61	18.3	21.1	80.8	93.0
$\ln(\mu) \times 10^{-5}$	23.0	26.2	2.46	2.8	1.05	1.19	1.7	1.94
$\ln(D_L) \times 10^{-3}$	43.7	231	6.67	34.9	1.15	5.88	0.553	2.78
ι	$2.80°$	$89.7°$	$0.413°$	$13.1°$	$0.0678°$	$2.17°$	$0.0324°$	$1.03°$
ψ	$3.86°$	$794°$	$0.575°$	$112°$	$0.105°$	$18.2°$	$0.0501°$	$8.61°$
γ_o	$7.96°$	$1589°$	$2.27°$	$226°$	$1.34°$	$37.1°$	$1.23°$	$18.0°$
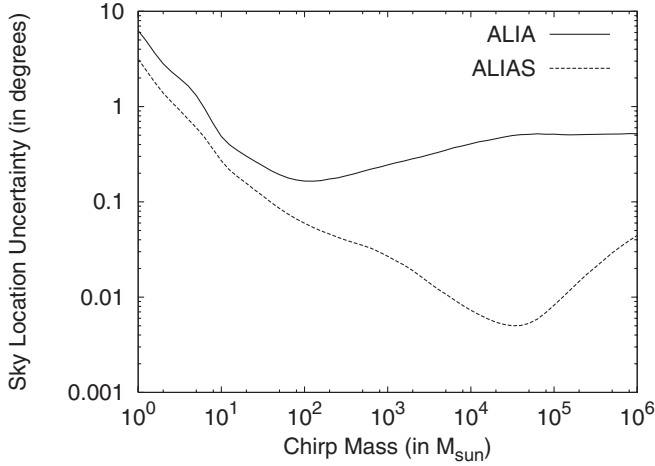
FIG. 6. Uncertainty in the sky location for both ALIA and ALIAS plotted against binary chirp mass. Binary system constituents in this plot have equal masses and are located at $z = 1$.

ALIA) by factors of 33, 23, 18, and 21, respectively. The parameters $\mathcal{M}$, μ, and γ_o only see a factor of ~ 2 improvement in resolution.

Comparing Fig. 7 with Fig. 6, one can see that the increased resolution in the luminosity distance corresponds with the increased precision in sky location due to their large covariance. A similar effect was seen in the work of Hughes and Holz [22], where the addition of electromagnetic information to fix the sky location of a BH merger resulted in a marked increase in resolution of the luminosity distance. In our case, the degeneracy is broken by the improved angular resolution afforded by the baseline between the ALIAS detectors. These improvements in sky location and luminosity distance resolution will provide an even more detailed three dimensional distribution of the IMBHs than that provided by ALIA. Increasing the 3D
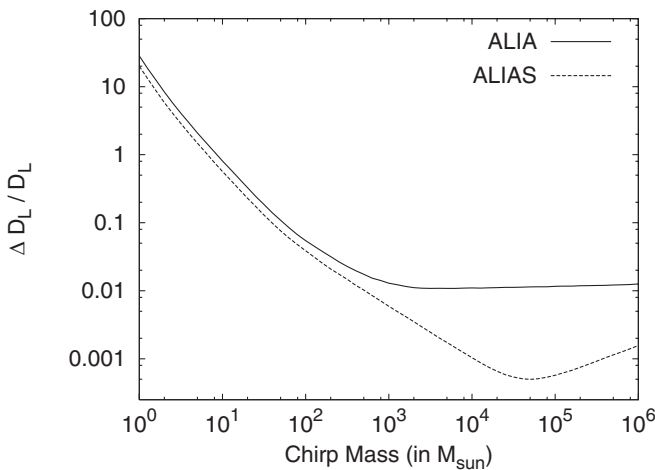

FIG. 7. Uncertainty in the luminosity distance of both ALIA and ALIAS plotted against binary chirp mass. Binary system constituents in this plot have equal masses and are located at $z = 1$.

resolution of the distribution of IMBHs by roughly a factor of 6 on the low end of the mass range ($50 M_\odot$) up to $\sim 200\,000$ on the high end of the mass range ($50\,000 M_\odot$), would provide much more detailed information compared to ALIA, with which to test theoretical predictions about IMBHs.

Figure 5 shows the SNR histogram for $10 M_\odot$ equal mass binaries for ALIA and ALIAS. While more than two-thirds of the sources at $z = 1$ would be positively detected, nearly one-third would be missed. However, these results suggest that ALIAS will be able to detect nearly all of the $10 M_\odot$ binaries with luminosity distances less than 3 Gpc. This is roughly in keeping with the general trend of ALIAS's capabilities compared to ALIA.

From Fig. 2 we saw that, for masses below $10 M_\odot$, the source's signal lies below the sensitivity curve for the week prior to coalescence. For larger masses, more of the binary's final chirp will be detectable. This is why the angular resolution of ALIAS becomes so much better than ALIA's at the upper end of the IMBH mass range. For masses above $10^5 M_\odot$, the final chirp occurs before the "sweet-spot" of the sensitivity curve, which diminishes ALIAS's advantage over ALIA.

C. Results for ALIA and ALIAS for unequal mass binaries

Equal mass binaries are the easiest to study, but they can give an overly optimistic picture of the instrument capabilities as they yield the smallest parameter uncertainties. To study this bias and provide a more realistic picture of the capabilities of ALIA and ALIAS, we now consider the case where the masses of each component in the binary are drawn from logarithmic distributions in the range 1–$10^8 M_\odot$. The results are still presented as a function of chirp mass, but the mass ratios reflect the underlying mass distribution.

Figure 8 shows the plot of sky location uncertainty against chirp mass. The uncertainties in sky location for masses above $10^2 M_\odot$ are larger than those shown in Fig. 6. The increase in sky angle uncertainty relative to the equal mass case was a factor of ~ 2 for ALIA. Similarly, other parameters show a factor of ~ 3 increase in their uncertainties relative to the equal mass study.

However, ALIAS still maintains an advantage in locating binaries. In fact, for chirp masses below $\sim 500 M_\odot$ the increase in precision for ALIAS over ALIA in locating unequal binaries is nearly the same as it was for equal mass binaries, a factor of roughly $\sqrt{2}$. At higher chirp masses we see less of a difference in angular resolution than in the equal mass study (factors of ~ 9 compared to ~ 90). This trend holds for t_c, D_L, ι, and ψ, which show maximum increases in precision ~ 4 for ALIAS over ALIA, while $\mathcal{M}$, μ, and γ_o show maximum increase in precision ~ 2 for ALIAS over ALIA (as they did for equal mass binaries). Thus the increased resolution in the 3D distribution of
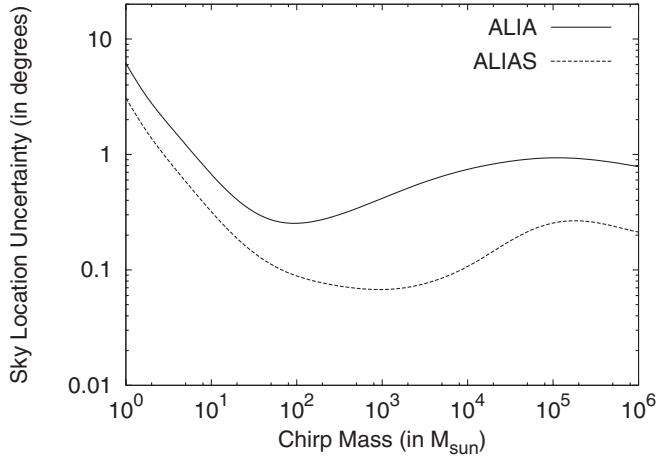
FIG. 8.   Uncertainty in the sky location for both ALIA and ALIAS plotted against binary chirp mass. Binary system constituents in this plot have unequal masses and are located at $z = 1$.

IMBHs for ALIAS over ALIA for unequal mass binaries ranges from a factor of ~ 6 up to ~ 300.

D. Results for LISA and LISAS

Figure 9 compares the sky location uncertainties for the LISA mission to the LISAS mission. As was seen with ALIA and ALIAS, the addition of a second constellation to LISA provides a marked increase in parameter resolution. The increases in parameter resolution for LISAS over LISA are similar to those found between ALIAS and ALIA. The angular resolution showed a maximum improvement of ~ 25 just above $10^5 M_\odot$. Also, a lesser benefit than that shown in Fig. 9 occurs in the t_c, D_L, ι, and ψ parameters (with factors of maximum increase ~ 12 just above $10^5 M_\odot$), while $\mathcal{M}$, μ, and γ_o show only a modest maximum improvement by a factor of ~ 2. Our results are
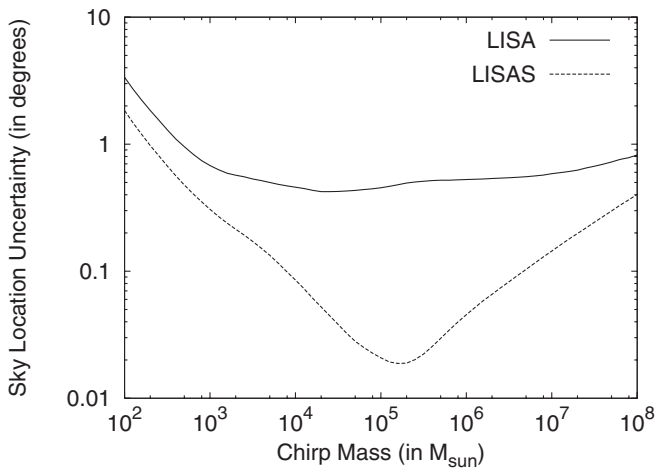

FIG. 9.   Uncertainty in the sky location for both LISA and LISAS plotted against binary chirp mass. Binary system constituents in this plot have equal masses and are located at $z = 1$.
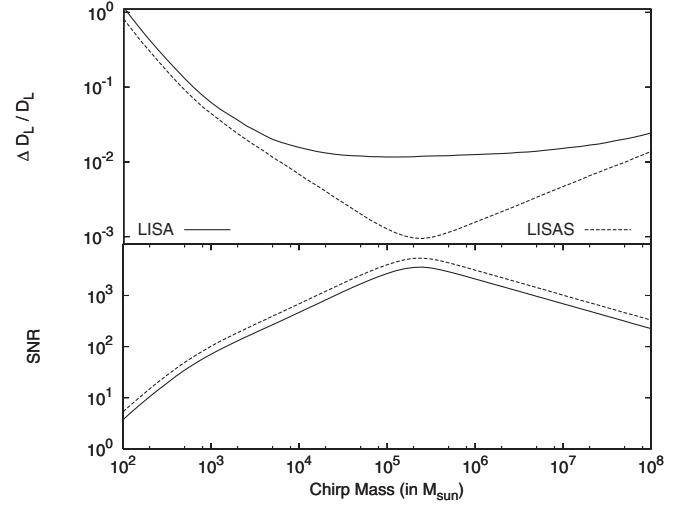

FIG. 10.   Uncertainty in the luminosity distance and the SNR for both LISA and LISAS plotted against binary chirp mass. Binary system constituents in this plot have equal masses and are located at $z = 1$.

in the same range as those found by Seto [23] for sources detected by LISA that have undergone strong gravitational lensing. In that case the extended baseline was provided by the time delay in the arrival of the signals, which effectively turned a single LISA detector into a LISAS system. Seto also gave brief consideration to the performance of a dual LISA mission, and found the ratio of angular resolution between LISAS and LISA to be larger than that seen in our simulations. The discrepancy can be traced to Seto including a large galactic confusion background which limits the time that the sources are in-band, thus magnifying the advantage of the dual configuration.

The shift in the placement of the minimum uncertainties, compared to ALIA and ALIAS, can be understood from Fig. 2. The signal from a $10^3 M_\odot$ equal mass binary is passing below the LISA sensitivity curve in the last week before coalescence, and before the final chirp of the binary. This is evident in Fig. 9, where the angular resolution of the single and dual configurations is similar for masses below $10^3 M_\odot$. The sweet-spot of the LISA sensitivity curve is at ~ 5 mHz, which is where $10^5 M_\odot$ binaries experience their final chirp. Above $10^5 M_\odot$, less of the final chirp occurs near the sweet-spot, and the difference in the angular resolution diminishes. Figure 10 shows how this shift corresponds precisely to the shift in the maximum SNR of the LISA and LISAS missions. The plot shows how the increase in the mean SNR ($\sqrt{2}$) is uniform across the range of chirp masses. Also, it shows again how the resolution in D_L improves with the addition of more information in the form of increased angular resolution.

E. Results for BBO

Table V summarizes the medians and means of the parameter uncertainties for detections of equal mass bi-

TABLE V. SNR and parameter uncertainties for BBO with sources at $z = 3$.

	$1.4M_\odot$		$10M_\odot$		$10^2M_\odot$	
	Median	Mean	Median	Mean	Median	Mean
SNR	156	162	809	843	4958	5189
Sky location	$3.31''$	$4.49''$	$0.673''$	$0.920''$	$0.176''$	$0.246''$
$\ln(t_c) \times 10^{-12}$	179	207	32.1	37.2	8.09	9.28
$\ln(\mathcal{M}) \times 10^{-9}$	63.1	72.7	7.02	8.09	30.4	35.0
$\ln(\mu) \times 10^{-6}$	173	200	16.3	18.8	4.97	5.70
$\ln(D_L) \times 10^{-3}$	28.9	150	5.58	29.1	0.927	4.73
ι	$1.86°$	$57.3°$	$0.360°$	$11.1°$	$0.0592°$	$1.78°$
ψ	$2.54°$	$497°$	$0.492°$	$96.1°$	$0.0806°$	$15.2°$
γ_o	$7.71°$	$996°$	$3.93°$	$194°$	$2.82°$	$32.3°$

naries with masses of $1.4M_\odot$, $10M_\odot$, and $10^2M_\odot$ for the BBO. Histograms for this data have the same general shapes as those shown in Fig. 4 and so are not shown.

As can be seen from the data, the BBO is an extremely sensitive detector. The SNRs show that if the BBO meets design specifications there will be positive detection of coalescing stellar mass binaries out to (indeed well beyond) a redshift of $z = 3$. Similarly, the BBO will provide a precise picture of coalescence rates, including how these rates relate to luminosity distance. With a combination of sky location and luminosity distance, the BBO should be able to pick out the host galaxy of the majority of coalescing binaries. Data taken by the BBO up to a month before coalescence (using 11 months of data) will determine t_c to within seconds, again providing ample warning time for other detectors to gather data on the coalescence.

F. Results for BBO Star

As can be seen in Fig. 2, the final chirp of solar mass or NS coalescing binaries occurs below the noise level of the BBO. Thus the outrigger constellations do not provide an extended baseline for the last few days of NS chirp.

TABLE VI. SNR and parameter uncertainties for BBO star constellations with sources at $z = 3$.

	$1.4M_\odot$		$10M_\odot$		$10^2M_\odot$	
	Median	Mean	Median	Mean	Median	Mean
SNR	96.9	114	484	598	3022	3697
Sky location	$82.6''$	$107''$	$214''$	$256''$	$516''$	$596''$
$\ln(t_c) \times 10^{-9}$	2.98	3.43	7.52	8.60	19.8	22.3
$\ln(\mathcal{M}) \times 10^{-8}$	13.1	15.1	2.00	2.29	6.95	7.92
$\ln(\mu) \times 10^{-5}$	3.70	4.28	3.70	4.31	1.23	1.53
$\ln(D_L) \times 10^{-3}$	49.9	257	12.5	68.0	6.51	31.9
ι	$3.02°$	$95.8°$	$0.767°$	$22.9°$	$0.310°$	$7.43°$
ψ	$4.07°$	$815°$	$1.04°$	$176°$	$0.529°$	$40.6°$
γ_o	$14.1°$	$1633°$	$9.56°$	$357°$	$6.99°$	$84.9°$

Positive detection of NS binaries at $z = 3$ can be accomplished with the initial deployment of the two constellations that make up the star, while still providing the cross-correlating needed to detect the GWB.

Table VI summarizes the medians and means of the parameter uncertainties for the detection of equal mass binaries with masses of $1.4M_\odot$, $10M_\odot$, and $10^2M_\odot$ for the BBO Star. Histograms for this data have the same general shapes as those shown in Fig. 4 and so are not shown.

Figure 11 plots the uncertainty in sky location against chirp mass for the BBO and BBO Star. As can be seen, the effect of the outrigger constellations is significant, providing for increased parameter resolution for the full BBO throughout the range of chirp masses shown, with a maximum increase of ~ 3700 around $200M_\odot$. Similar to the ALIA/ALIAS comparison, this extra precision increases until all of the final chirp lies above the sensitivity curve (see Fig. 2), and begins to decrease as less and less of the final chirp occurs in the frequency range of the sweet-spot of the sensitivity curve (which for BBO is ~ 1 mHz). The improvement in the mean SNR for BBO over BBO Star is the expected $\sqrt{2}$. Also, the improvement in the resolution of t_c (~ 3550) is comparable to that seen in the angular resolution. More modest increases occur for D_L, ι, and ψ, which increase by factors of 52, 35, and 47, respectively. Only slight (~ 2.5) increases are seen for $\mathcal{M}$, μ, and γ_o.

The SNRs from BBO Star are sufficient for positive detection of binaries with constituents less than one solar mass out to, and beyond, $z = 3$. While the full BBO offers considerable advantages for doing precision gravitational wave astronomy, BBO Star could fulfill the main science objective of detecting the cosmic gravitational wave background (CGB) while still providing useful information about binary populations.
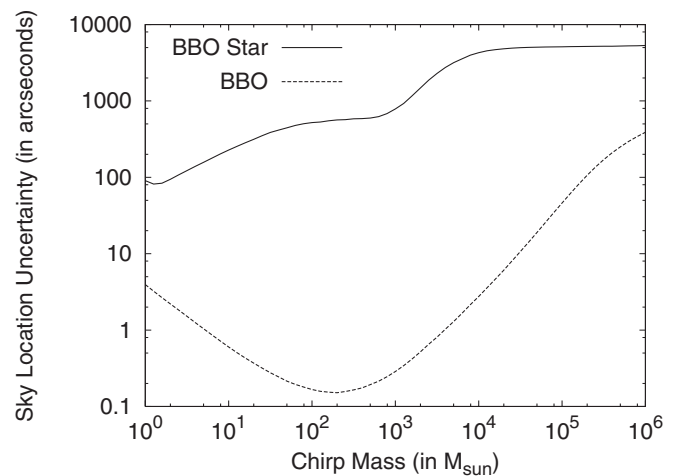

FIG. 11. Uncertainty in sky location versus chirp mass for the standard BBO design and the star constellations of the BBO. Binary system constituents in this plot have equal masses and are located at $z = 3$.

V. CONCLUSION/DISCUSSION

While our survey is by no means comprehensive, it has helped to map out the science that can be done with the ALIA and BBO missions. We have shown that ALIAS, a modest extension to the ALIA mission, would be able to return a far more accurate census of the IMBH population. In addition we have shown that a similar extension to LISA would greatly improve its ability to locate the host galaxies of coalescing binaries. On the other hand, if we are willing to give up some of the precision astronomy offered by the full BBO, we could get by with just the first phase of the BBO deployment. The BBO Star configuration could satisfy the primary goal of detecting the CGB, while still providing a detailed binary census.

ACKNOWLEDGMENTS

[1] P. L. Bender *et al.*, MPQ 233, 1998.

[2] D. Hils, P. L. Bender, and R. F. Webbink, Astrophys. J. **360**, 75 (1990).

[3] C. Cutler, Phys. Rev. D**57**, 7089 (1998).

[4] T. A. Moore and R. W. Hellings, Phys. Rev. D**65**, 062001 (2002).

[5] R. Takahashi and N. Seto, Astrophys. J. **575**, 1030 (2002).

[6] J. Crowder and N. J. Cornish, Phys. Rev. D **70**, 082004 (2004).

[7] S. A. Hughes, Mon. Not. R. Astron. Soc. **331**, 805 (2002).

[8] N. Seto, Phys. Rev. D **66**, 122001 (2002).

[9] A. Vecchio, Phys. Rev. D **67**, 022001 (2003).

[10] L. Barack and C. Cutler, Phys. Rev. D **69**, 082005 (2004).

[11] P. L. Bender, P. J. Armitage, M. C. Begelman, and R. Pema, Massive Black Hole Formation and Growth, White Paper submitted to the NASA SEU Roadmap Committee, 2005.

[12] S. Phinney *et al.*, The Big Bang Observer: Direct Detection of Gravitational Waves from the Nirth of the Universe to the Present, NASA Mission Concept Study, 2004.

[13] N. J. Cornish and S. L. Larson, Classical Quantum Gravity **18**, 3473 (2001).

[14] A. Farmer and S. Phinney, Mon. Not. R. Astron. Soc. **346**, 1197 (2003)

[15] L. Blanchet, B. R. Iyer, C. M. Will, and A. G. Wiseman, Classical Quantum Gravity **13**, 575 (1996).

[16] M. Tinto and J. W. Armstrong, Phys. Rev. D **59**, 102003 (1999).

[17] T. A. Prince, M. Tinto, S. L. Larson, and J. W. Armstrong, Phys. Rev. D **66**, 122002 (2002).

[18] L. Rubbo, N. J. Cornish, and O. Poujade, Phys. Rev. D **69**, 082003 (2004).

[19] R. Nayak, A. Pai, S. V. Dhurandhar, and J.-Y. Vinet, Classical Quantum Gravity **20**, 1217 (2003).

[20] D. N. Spergel *et al.*, Astrophys. J. Suppl. Ser. **148**, 175 (2003).

[21] B. Kocsis, Z. Frei, Z. Haiman, and K. Menou, astro-ph/0505394 [Astrophys.J. (to be published)].

[22] S. A. Hughes and D. E. Holz, Classical Quantum Gravity **20**, S65 (2003).

[23] N. Seto, Phys. Rev. D**69**, 022002 (2004).